Landau level quantization and almost flat modes in three-dimensional semimetals with nodal ring spectra

Jun-Won Rhim[1] and Yong Baek Kim[2,3]
[1]*School of Physics, Korea Institute for Advanced Study, Seoul 130-722, Korea*
[2]*Department of Physics, University of Toronto, Toronto, Ontario, Canada M5S 1A7*
[3]*Canadian Institute for Advanced Research, Toronto, Ontario, Canada M5G 1Z8*
(Received 12 May 2015; published 28 July 2015)

We investigate Landau level structures of semimetals with nodal ring dispersions. When the magnetic field is applied parallel to the plane in which the ring lies, there exist almost nondispersive Landau levels at the Fermi level ($E_F = 0$) as a function of the momentum along the field direction inside the ring. We show that the Landau levels at each momentum along the field direction can be described by the Hamiltonian for the graphene bilayer with fictitious interlayer couplings under a tilted magnetic field. Near the center of the ring where the interlayer coupling is negligible, we have Dirac Landau levels which explain the appearance of the zero modes. Although the interlayer hopping amplitudes become finite at higher momenta, the splitting of zero modes is exponentially small and they remain almost flat due to the finite artificial in-plane component of the magnetic field. The emergence of the density of states peak at the Fermi level would be a hallmark of the ring dispersion.

DOI: 10.1103/PhysRevB.92.045126 PACS number(s): 71.55.Ak, 71.70.Di, 72.80.Ga

I. INTRODUCTION

Semimetals, usually the reflection of unconventional electronic structures at the Fermi surface (FS), are related to various anomalous properties and/or exotic phases such as the unconventional quantum Hall effect (QHE) in graphene systems [1–4], a pressure-induced anomalous Hall effect in the Weyl semimetal (SM) [5], and a non-Fermi-liquid phase and peculiar quantum oscillations in the quadratic band-touching SM [6–10]. Also, in many cases, they are classified as topologically nontrivial metals involving surface states [11–16] which are generalizations of the concept of the topological insulator [17] to the metallic systems [18].

Recently, there have been many suggestions for the novel semimetals with nodal ring FSs with different topological classification schemes [19–28]. Their topological nontriviality ensures the existence of surface modes protected by inversion, time-reversal, or certain lattice symmetries. Since those candidate materials for the nodal ring semimetal (NRS) have been proposed very recently, the investigations of their physical properties and experimental observations are still outstanding open problems.

In this paper, we demonstrate that the NRSs exhibit unusual three-dimensional (3D) Landau level structures when the magnetic field is applied parallel to the plane of the ring. Noticing that the low energy Hamiltonians for various NRSs have the same generic structure, we employ the continuum model for $SrIrO_3$ as an example of the NRS. It is explained later that our results are generic and can be applied to other materials as well. We show that the NRS's Landau levels simulate the adiabatic transition from two decoupled graphenes to a Bernal stacked graphene bilayer under a magnetic field with an artificial parallel component as a function of the conserved momentum. During that process, almost flat Dirac zero modes are found inside the nodal ring. For some parameters, not far from the realistic ones, a 3D quantum Hall effect (QHE) may occur with a little doping. Also, we suggest that the nodal ring can be probed by the measurements of density of states (DOS) under the magnetic field.

II. THE CONTINUUM MODEL FOR A NODAL RING SEMIMETAL

We consider the continuum limit of the tight binding (TB) model for $SrIrO_3$ near the U point [$\mathbf{k}_U = (0, -\pi, \pi)$] in the Brillouin zone [Fig. 1(a)],

$$\mathcal{H}^U = 2t_0 q_b \tau_x - t_0 q_c \nu_x - t_1 q_b \tau_y \sigma_z - \frac{t_3 q_a}{2} \nu_z \tau_y (\sigma_x + \sigma_y) + \left(\frac{t_2 q_c}{2} \nu_y \tau_z - \frac{t_4 q_b}{2} \nu_z \tau_y + t_5 \nu_x \tau_y \right) (\sigma_x - \sigma_y), \quad (1)$$

where $\mathbf{q} = \mathbf{k} - \mathbf{k}_U$ and a,b,c represent orthorhombic directions of the lattice. Here, σ_α, τ_α, and ν_α are Pauli matrices, where σ_α is for the $J_{\text{eff}} = 1/2$ Kramers doublet and $\tau_\alpha(\nu_\alpha)$ is for the sublattices B and R (Y and G) [20]. The realistic TB parameters are known as $t_0 = -0.6$, $t_1 = -0.15$, $t_2 = 0.13$, $t_3 = -0.2$, $t_4 = 0.4$, and $t_5 = 0.06$ in eV. We consider, however, a wide range of TB parameters since we are interested in the generic properties of NRSs. The details of the TB model for $SrIrO_3$ are described in Appendix A.

$\mathcal{H}^U$ has both time-reversal and chiral symmetry ($\mathcal{C} = \sigma_z \nu_y \tau_z$). As a result, we have particle-hole symmetric, doubly degenerate dispersion relations as follows,

$$E^U_{\zeta,\zeta'}(\mathbf{q}) = \zeta \left\{ (v_a q_a)^2 + (v_b q_b)^2 + (v_c q_c)^2 + 2t_5^2 + \zeta' \left\{ 8t_5^2 [(v_a q_a)^2 + (v_c q_c)^2] + v_d^4 q_b^2 q_c^2 \right\}^{\frac{1}{2}} \right\}^{\frac{1}{2}}, \quad (2)$$

where $v_a = |t_3|/\sqrt{2}$, $v_b = \sqrt{[t_4^2 + 2(4t_0^2 + t_1^2)]/2}$, $v_c = \sqrt{(2t_0^2 + t_2^2)/2}$, $v_d = \{4(v_b v_c)^2 - 2t_0^2(t_4 - 2t_2)^2\}^{1/4}$, and $\zeta, \zeta' = \pm 1$. Near the U point, they are in good agreement with those of the original TB model, as compared in Figs. 1(c) and 1(d). In the continuum model, the nodal ring is just an ellipse, satisfying

$$4t_5^2 = t_3^2 q_a^2 + (2t_0^2 + t_2^2) q_c^2, \quad (3)$$

with major and minor radii given by $r_a = 2|t_5/t_3|$ and $r_c = 2|t_5|/(2t_0^2 + t_2^2)^{1/2}$. The ring exists unless $t_3 = 0$ or $t_0 = t_2 = 0$. Since the dispersion around the ring is linear along the radial

 ©2015 American Physical Society

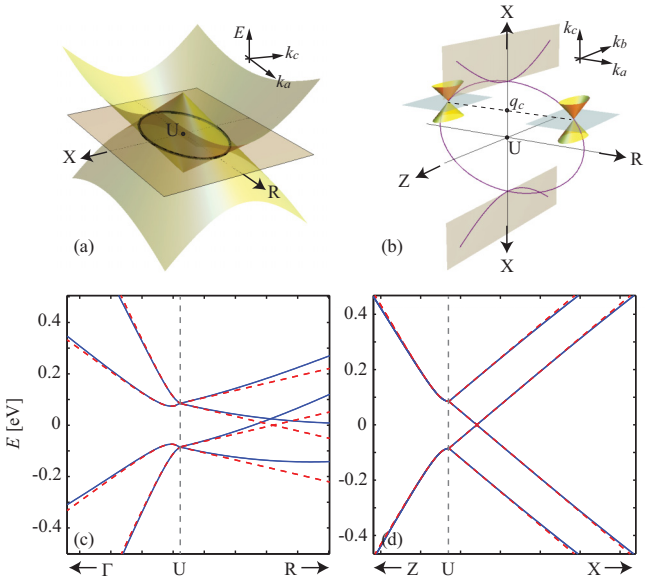

FIG. 1. (Color online) (a) Low energy band structures on the $k_b = -\pi$ plane where the nodal ring (black ellipse) resides. (b) The nodal chain appears when $2t_2 = t_4$. Two coupled doubly degenerate Dirac cones reside at the points where the nodal lines intersect the plane for given q_c. In (c) and (d), we compare energy spectra around the U point calculated from the full tight binding Hamiltonian (solid) and the continuum model $\mathcal{H}^U$ (dashed).

and k_b direction while constant along the nodal line, the DOS is proportional to energy and vanishing at the Fermi level. Interestingly, when $2t_2 = t_4$, we have extra nodal lines for $|q_c| > r_c$ in the $k_a = 0$ plane characterized by a hyperbolic curve,

$$4t_5^2 = (2t_0^2 + t_2^2)q_c^2 - 2(4t_0^2 + t_1^2 + 2t_2^2)q_b^2, \tag{4}$$

as depicted in Fig. 1(b). We call those consecutively occurring nodal lines the nodal chain. While those results are valid only around the U point, one can observe the nodal chain structure in the full TB model when it respects the chiral symmetry $\{\mathcal{H}^{\rm TB}, \mathcal{C}\} = 0$, which is realized when $t_{xy} = t_d = 0$.

III. NUMERICAL ANALYSIS OF LANDAU LEVEL QUANTIZATION

Now, we consider the Landau level quantization of the NRS. We assume that the magnetic field is applied along the c direction so that it is parallel to the plane of the ring. We neglect the Zeeman splitting ($\sim 10^{-4} B$ [T] eV) [29] since it is much smaller than the Landau level spacings of this system, which is order of 10 meV when $B = 1$ T, as will be shown later.

Using the quantization scheme $q_a = (a + a^\dagger)/\sqrt{2} l_{\rm B}$ and $q_b = i(a - a^\dagger)/\sqrt{2} l_{\rm B}$, the Landau level wave function is expressed in the form $\Psi = \sum_{n=0}^{\infty} (c_n^{B\uparrow}, c_n^{R\uparrow}, c_n^{Y\uparrow}, c_n^{G\uparrow}, c_n^{B\downarrow}, c_n^{R\downarrow}, c_n^{Y\downarrow}, c_n^{G\downarrow})^{\rm T} u_n$, where u_n is the simple harmonic oscillator (SHO) eigenfunction [10]. If we separate the eigenvector into two pieces as $\mathbb{A}_n = (c_n^{B\uparrow}, c_n^{R\uparrow}, c_n^{B\downarrow}, c_n^{R\downarrow})^{\rm T}$ and $\mathbb{B}_n = (c_n^{Y\uparrow}, c_n^{G\uparrow}, c_n^{Y\downarrow}, c_n^{G\downarrow})^{\rm T}$, they satisfy the following coupled secular

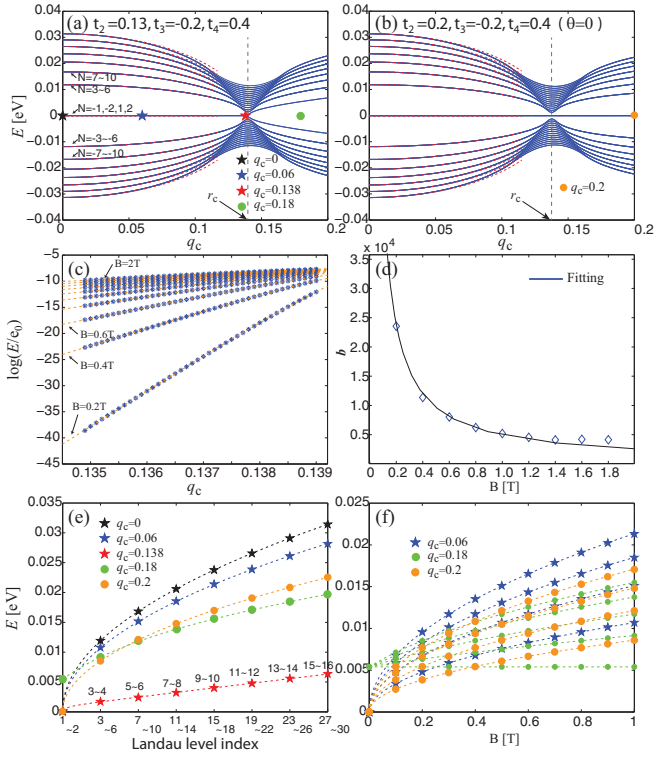

FIG. 2. (Color online) (a), (b) Landau levels of the NRS as functions of q_c for different TB parameters when the magnetic field ($B = 1$ T) is along the c direction. Blue solid lines are numerical results while red dashed curves are analytic ones obtained from the fictitious graphene bilayer model near $q_c = 0$. (c) Central Landau levels ($N = 1,2$) near $q_c = r_c$ ($*$) which are fitted by a formula $\varepsilon \sim \pm(1 - aq_c^2)^\alpha q_c^\beta \exp(bq_c^2)$ for various magnetic fields (red dashed lines). $e_0 = 1$ eV. (d) b in the exponent of the fitting function and its fitting by $b_0 l_{\rm B}^2$. (e), (f) Landau levels as functions of the Landau level index and magnetic field for some momenta.

equations,

$$\varepsilon \mathbb{A}_n = \sqrt{n+1}\mathbf{M}_+ \mathbb{A}_{n+1} + \mathbf{L}_+ \mathbb{B}_n + \sqrt{n}\mathbf{M}_+^\dagger \mathbb{A}_{n-1}, \tag{5}$$

$$\varepsilon \mathbb{B}_n = \sqrt{n+1}\mathbf{M}_- \mathbb{B}_{n+1} + \mathbf{L}_- \mathbb{A}_n + \sqrt{n}\mathbf{M}_-^\dagger \mathbb{B}_{n-1}, \tag{6}$$

where

$$\mathbf{M}_\zeta = \sum_{m=1}^{2} \frac{i t_{m-1}}{2^{m-\frac{3}{2}} l_{\rm B}} \mathbf{\Gamma}_{m5} - \zeta \sum_{n=3}^{4} \frac{(-1)^m t_3 - i t_4}{2\sqrt{2} l_{\rm B}} \mathbf{\Gamma}_{1n}, \tag{7}$$

$$\mathbf{L}_\zeta = -t_0 q_c - \zeta \frac{i t_2 q_c}{2} (\mathbf{\Gamma}_{45} - \mathbf{\Gamma}_{35}) - t_5 (\mathbf{\Gamma}_{14} - \mathbf{\Gamma}_{13}). \tag{8}$$

Here, we adopt the representations of the Dirac gamma matrices in Ref. [30]. The coefficient is assumed to be zero when its subscript n is negative.

By solving the above equations numerically, we plot the Landau level spectra as functions of the conserved momentum q_c in Figs. 2(a) and 2(b). Strictly speaking, each band is only doubly degenerate, but one can see almost fourfold degeneracies inside the ring away from the vicinity of its edge at $q_c = r_c$. We label them by the nonzero integer N in such a way that levels with positive (negative) energies are marked

by positive (negative) integers in increasing (decreasing) order from the central ones near zero energy.

We observe doubly degenerate two bands which are almost flat near zero energy inside the nodal ring ($q_c < r_c$). Those flat bands are fitted nicely by a formula

$$\varepsilon \sim \pm\left(1 - aq_c^2\right)^{\alpha} q_c^{\beta} \exp\left(bq_c^2\right) \tag{9}$$

near the ring's edge, as shown in Fig. 2(c). The exponent's coefficient b is found to be approximated as $1.886 l_B^2$, as plotted in Fig. 2(d). As a result, the energies of central Landau levels ($N = \pm 1,2$) rapidly reduce to zero as we go inside the ring from $q_c = r_c$ by an amount of $\delta q_c \sim 1/(r_c l_B^2)$. While the splitting between those flat modes becomes finite outside the ring ($q_c > r_c$), the only exception is when $2t_2 = t_4$, for which we have four zero modes for any value of q_c.

In addition, we find that, when q_c is well inside the ring, our Landau level spectra are Dirac-like, as shown in Figs. 2(e) and 2(f). The energies are proportional to the square root of the Landau level index and magnetic field. On the other hand, the dispersions cannot be fitted by the Dirac Landau levels and show linear behaviors for large Landau level indices and magnetic fields if q_c is close to the ring's boundary or outside the ring. However, when the nodal chain appears for $2t_2 = t_4$, one can have Dirac Landau levels again for larger q_c.

IV. INTERPRETATION VIA GRAPHENE BILAYER UNDER A TILTED MAGNETIC FIELD

To understand the nature of the peculiar Landau level structures of the NRS, we introduce a unitary transformed Hamiltonian $\mathcal{H}^D$ which is in a block-diagonalized form of two 4×4 submatrices. Since it gives us exactly the same band structures and Landau levels, it can be regarded as a unitary transform of $\mathcal{H}^U$. Those two submatrices of $\mathcal{H}^D$ are given by

$$\mathcal{H}^D_{K(K')} = \begin{pmatrix} \mathbf{h}^{+}_{K(K')} & \mathbf{g}_\theta \\ \mathbf{g}^{\dagger}_\theta & \mathbf{h}^{-}_{K(K')} \end{pmatrix}, \tag{10}$$

where

$$\mathbf{h}^{\zeta}_{K(K')} = v_a(q_a - \zeta p_a)\mu_x \pm v_b q_b \mu_y, \tag{11}$$

$$\mathbf{g}_\theta = v_c q_c(\mu_x - i\cos\theta\mu_y - i\sin\theta\mu_z) \tag{12}$$

for $q_c \leqslant r_c$, and

$$\mathbf{h}^{\zeta}_{K(K')} = v_a q_a \mu_x \pm v_b(q_b - \zeta p_b)\mu_y + \zeta m_0 q_c \mu_z, \tag{13}$$

$$\mathbf{g}_\theta = \sqrt{2} t_5 \mu_x \tag{14}$$

for $q_c > r_c$. Here, μ_α is the Pauli matrix and the plus-minus sign denotes the $K(K')$ valley. $\mathbf{h}^{\zeta}_{K(K')}$ is the Dirac Hamiltonian with the dispersions centered at $\mathbf{q} = (\zeta p_a, 0, q_c)$ for $q_c \leqslant r_c$ and $\mathbf{q} = (0, \zeta p_b, q_c)$ for $q_c > r_c$ where $p_a = \sqrt{[2t_5^2 - (v_c q_c)^2]/v_a^2}$ and $p_b = v_d^2 q_c / 2v_b^2$. When $q_c > r_c$, we have the mass term with

$$m_0 = \sqrt{v_c^2 - v_d^4/4v_b^2} = v_c \sin\theta, \tag{15}$$

while it is massless inside the ring. In the mixing term $\mathbf{g}_\theta$, $\cos^2\theta = v_d^4/4(v_b v_c)^2$. The transformed Hamiltonian gives us exactly the same energy spectra in Eq. (2).

Since $\mathbf{h}^{\zeta}_{K}$ and $\mathbf{h}^{\zeta}_{K'}$ are the Dirac Hamiltonians at different valleys K and K', one can interpret $\mathcal{H}^D$ as a Hamiltonian of a graphene bilayer with a fictitious interlayer coupling $\mathbf{g}_\theta$. Here, $\zeta = +$ and $-$ correspond to the upper and lower layer of the artificial graphene bilayer and we denote its basis as $\psi = (c_{A_+}, c_{B_+}, c_{A_-}, c_{B_-})^{\mathrm{T}}$. Furthermore, the position of Dirac points in the upper and lower layer are shifted in opposite directions. For instance, inside the ring ($q_c < r_c$), two Dirac cones are placed at $\mathbf{q} = (p_a, 0, q_c)$ and $(-p_a, 0, q_c)$ in the $q_c = \text{const}$ plane in the upper and lower layer of the graphene bilayer, as shown in Fig. 1(b). This kind of shift can be realized when the magnetic field is applied parallel to graphene layers with strength $B_\parallel = 2\hbar p_a / ed$, where d is the interlayer distance [31,32]. This fictitious parallel magnetic field has its maximum value at the ring's center ($q_c = 0$) and vanishes at the ring's boundary ($q_c = r_c$). The system transforms from two copies of graphene monolayers to a graphene bilayer with interlayer coupling $\mathbf{g}_\theta$ as increasing q_c since $\mathbf{g}_\theta$ is proportional to q_c.

Applying the magnetic field along the c direction, we obtain the Landau level dispersions numerically and find that they are exactly the same as the ones from $\mathcal{H}^U$. Now, we discuss detailed properties of the Landau level spectra of the NRS.

(i) Deep inside the ring ($q_c \ll r_c$), the Landau level of the NRS at each q_c can be considered as those of the four independent anisotropic Dirac particles. When $q_c = 0$, $\mathbf{g}_\theta$ vanishes and we have four decoupled anisotropic Dirac Hamiltonians. In this case, the Landau level spectrum is

$$\varepsilon^{\pm}_m = \pm v_f l_B^{-1} \sqrt{2m}, \tag{16}$$

with fourfold degeneracy where m is an integer and $v_f = (v_a v_b)^{1/2}$. To be precise, one has exact zero modes only at $q_c = 0$. However, the Dirac-like feature is maintained up to quite large momenta where $\mathbf{g}_\theta$ is finite because the mixing between wave functions on two Dirac cones is exponentially small ($\sim e^{-p_a^2 l_B^2}$), with the distance between two Dirac cones $2p_a$ being maximized at $q_c = 0$. In this regime, the main role of the finite coupling $\mathbf{g}_\theta$ is the renormalization of the Fermi velocity. One can project out the contribution of the lower layer and construct an effective low energy Hamiltonian around the Dirac point of the upper layer by using the resolvent $(\varepsilon - \mathbf{h}^{-}_{K(K')})^{-1}$ [4,33]. This gives us a generalized eigenvalue problem of the form

$$\varepsilon \mathbf{S}_\theta \psi_+ = (\mathbf{h}^{+}_{K(K')} - (2v_a p_0)^{-2} \mathbf{g}_\theta \mathbf{h}^{-}_{K(K')} \mathbf{g}^{\dagger}_\theta)\psi_+, \tag{17}$$

where $\mathbf{S}_\theta = \mathbf{I} + (2v_a p_0)^{-2} \mathbf{g}_\theta \mathbf{g}^{\dagger}_\theta$, $\mathbf{I}$ is an identity matrix, and ψ_+ is the wave function for the upper layer. For an intuitive picture, let us focus on the case $\theta \ll 1$. Notice that the realistic TB parameters ($t_2 = 0.13$, $t_3 = -0.2$, and $t_4 = 0.4$) correspond to this limit ($\cos\theta = 0.9969$). After a transformation to an orthonormal basis set [34], we arrive at a quite simple form of the effective Hamiltonian for the upper layer, $[1 + (v_c q_c / v_a p_a)^2]^{-1/2} \mathbf{h}^{+}_{K(K')}$, with the renormalized Fermi velocity

$$v'_f = \left\{1 + \left(\frac{v_c q_c}{v_a p_a}\right)^2\right\}^{-\frac{1}{2}} v_f. \tag{18}$$

In Figs. 2(a) and 2(b), we show by the red dashed lines that the Dirac Landau levels with the renormalized Fermi velocity have good agreements with the numerics when $q_c \ll r_c$.

(ii) We have, as shown in Fig. 2(b), four exact zero modes for arbitrary q_c when $\theta = 0$ ($2t_2 = t_4$), where $\mathbf{g}_\theta$ has only the interlayer coupling $2v_c q_c$ between the A_- and B_+ sites. In this case, our fictitious model is exactly the same as the graphene bilayer with Bernal stacking under a parallel magnetic field. Although we must rely on the numerics to analyze all Landau levels due to the fictitiously tilted magnetic field, one can show that we have exact zero modes for arbitrary momentum q_c. Here, to avoid unnecessary complexity, we only provide analytic solutions for the case $q_c < r_c$. See Appendix B for other cases. We define the ladder operator for the upper ($\zeta = +1$) and lower ($\zeta = -1$) layer as

$$a_\zeta = \frac{l_B}{\sqrt{2}v_f}[v_a(q_a - \zeta p_a) + i v_b q_b], \tag{19}$$

which satisfy $a_+ = a_- - \sqrt{2}v_a l_B p_a/v_f$. They have their own SHO eigenfunctions u_n^- and u_n^+ which are shifted spatially from each other in the b direction. In this case, one can find four zero-energy eigenvectors as

$$\psi^0_{K,1} = \begin{pmatrix} u_0^+ \\ 0 \\ 0 \\ 0 \end{pmatrix} \quad \text{and} \quad \psi^0_{K,2} = c_0 \begin{pmatrix} u_0^- \\ 0 \\ \gamma_0 u_0^- \\ 0 \end{pmatrix} \tag{20}$$

for the K valley, and

$$\psi^0_{K',1} = \begin{pmatrix} 0 \\ 0 \\ 0 \\ u_0^- \end{pmatrix} \quad \text{and} \quad \psi^0_{K',2} = c_0 \begin{pmatrix} 0 \\ -\gamma_0 u_0^+ \\ 0 \\ u_0^+ \end{pmatrix} \tag{21}$$

for the K' valley, where $\gamma_0 = p_a v_a/(v_c q_c)$ and $c_0 = (1 + \gamma_0^2)^{-1/2}$ is the normalization factor. One can also find the analytic form of the eigenfunctions at the zero energy for $q_c \geqslant r_c$ in a similar way. The reason why we still have zero modes outside the ring is that we have four massless Dirac cones along the hyperbolic nodal line in the $k_a = 0$ plane [Fig. 1(b)] since $m_0 = 0$ for $\theta = 0$ [35].

(iii) On the other hand, the fourfold symmetry of the zero modes is broken for nonzero θ although the splitting between them is almost negligible. By using the zero-energy solutions inside the ring, we estimate their splitting for finite θ near $q_c = 0$ as

$$\begin{aligned} \Delta &\approx 2\left|\langle\psi^0_{K(K'),1}\left|\left[\mathcal{H}^D_{H(K')}(\theta) - \mathcal{H}^D_{K(K')}(0)\right]\right|\psi^0_{K(K'),2}\rangle\right| \\ &= d_0 q_c \left(1 - a_0 q_c^2\right)^{\frac{1}{2}} \exp\left(-b_0 q_c^2\right), \end{aligned} \tag{22}$$

where $a_0 = v_c^2/(2t_5^2)$, $b_0 = v_c^2 l_B^2/v_a^2$, and $d_0 = v_c \exp(-2t_5^2 l_B^2/v_a^2)$. The splitting of the lowest Landau level is extremely small near $q_c = 0$ and looks almost flat due to the factor l_B^2 in the exponent of d_0, which reflects the effect of the huge fictitious parallel magnetic field near $q_c = 0$. The derivation of the above is only valid around $q_c = 0$, where the mixing from higher Landau levels is minimal so that the projection onto the central Landau levels is safe. However, inspired by this formula, we could obtain the fitting function for the bands near the ring's edge, as shown in Fig. 2(c).

(iv) At $q_c = r_c$ and $\theta = 0$, where $B_\parallel = 0$, the situation becomes the usual Bernal stacked graphene bilayer under the perpendicular magnetic field, and the Landau levels are evaluated as

$$\varepsilon_n^{\zeta,\zeta'} = \zeta'\sqrt{2}v_c q_c \sqrt{\lambda_{1,n} + \zeta\sqrt{\lambda_{2,n} + \omega^4}}, \tag{23}$$

where $\lambda_{m,n} = 1 + m(2n-1)\omega^2$ and $\omega^2 = v_f^2/(2v_c^2 q_c^2 l_B^2)$. The Landau levels near the Fermi level are described by $\varepsilon_n^{-,\xi}$. In the low energy regime, it is approximated to

$$\varepsilon_n^{-,\xi} \approx \xi \frac{v_f^2}{v_c q_c l_B^2}\sqrt{n(n-1)}, \tag{24}$$

which is the well-known Landau levels of a graphene bilayer [4].

V. 3D QUANTUM HALL EFFECT

One of the interesting results for the $\theta = 0$ case [Fig. 2(b)] is that the zero-energy flat modes are separated from other bands with a finite gap. In this case, one can have the 3D QHE by a slight doping, as indicated by Halperin [36]. He showed that the conductivity tensor should be in the form of

$$\sigma_{ij} = \frac{e^2}{2\pi h}\epsilon_{ijk}G_k, \tag{25}$$

where ϵ_{ijk} is the Levi-Civita symbol and $\mathbf{G}$ is the reciprocal vector [36,37]. When $q_c = 0$ and $q_c = r_c$, the Hall conductance in the ab plane is given by $\sigma^{2D}_{ab} = 2e^2/h$ since our model is equivalent to the decoupled spinless graphene layers and the Bernal stacked graphene bilayer, respectively. As we do not have any gap closing, the Hall conductances at other momenta are also $\sigma^{2D}_{ab} = 2e^2/h$ due to the adiabatic continuation. Then, the three-dimensional Hall conductance is evaluated as

$$\sigma_{ab} = \int \frac{dq_c}{2\pi}\sigma^{2D}_{ab} = \frac{e^2}{2\pi h}\frac{4\pi}{a_c}, \tag{26}$$

where a_c is the lattice constant along the c direction. In the real material, it is expected that $\theta \neq 0$ and also there may be other electron or hole pockets at the Fermi level. In this case, we expect that the Hall conductance would be order of $\sim e^2/ha_c$ even though it is not strictly quantized. Further, we expect the strain effect may be used to tune the TB parameters close to the ideal case of the above.

VI. CONCLUSIONS AND DISCUSSIONS

We have studied the Landau level structures of the nodal ring semimetal based on the continuum Hamiltonian of $SrIrO_3$. We identified almost flat Landau levels at the Fermi level as a function of the momentum along the field direction, which are unusual in 3D systems. We were able to reveal the origin of their appearance by the analogy of the graphene bilayer with fictitious interlayer interactions under a tilted magnetic field. Inside the ring, the overlap between the wave functions at the different Dirac points diminishes exponentially due to the parallel component of the artificial magnetic field. As a result, continuous series of Dirac cones on the ring provide

us with almost zero modes inside the ring while we have an exponentially increasing Landau level splitting only in the vicinity of the ring's edge. For a certain choice of the tight binding parameters, it was found that there are extra nodal lines outside the ring which also have Dirac characters. In this case, we have exact zero modes throughout the whole Brillouin zone and the 3D QHE might be realized.

Although we used a continuum model for $SrIrO_3$, the flat 3D Landau levels at the Fermi energy can be found in any semimetals with nodal ring dispersion, where the energy spectra are linear along the perpendicular directions of the nodal line so that one can find Dirac cones for a given momentum parallel to the ring's plane, as shown in Fig. 1(b). Recently, other candidate materials for the NRSs with the above properties have been suggested, such as Cu_3NZn, Cu_3NPd [22,27], Ca_3P_2 [23], LaN [24], and so on [25–27]. For example, the low energy Hamiltonian of Cu_3NZn, for a given q_y [$\mathbf{q}_\perp = (q_x, q_y)$], is given by

$$H \sim 2b_\perp q_0(q_x - q_0)\tau_z + v q_r \tau_y, \tag{27}$$

where $q_0 = \pm(-\Delta\epsilon/b_\perp - q_y^2)^{1/2}$ are the positions of two Dirac cones. It is also noticed that Ca_3P_2 has similar electronic structures from the band crossings along $M\Gamma K$ and the linear DOS around the nodal ring. Among these, Ca_3P_2 may be the most promising since its ring is free from other electron or hole pockets and has a sizable radius. Flat Dirac Landau levels would appear in these systems when the magnetic field is applied in the direction of the ring's plane. Because the flat bands have prominent peaks in the DOS, one might identify the existence of the nodal ring by scanning tunneling microscopy, even if it is buried in other dispersive bands.

ACKNOWLEDGMENTS

This work was supported by the NSERC of Canada, the CIFAR, and the Center for Quantum Materials at the University of Toronto. We thank Y. Chen, H.- Y. Kee, H.-S. Kim, and J. Kim for useful discussions.

APPENDIX A: TIGHT BINDING HAMILTONIAN OF $SrIrO_3$

Recently, the electronic structure of $SrIrO_3$ was studied by first principles calculations [19,20]. The corresponding tight binding model was found to be

$$\begin{aligned}\mathcal{H}^{\mathrm{TB}} = &\left(\varepsilon^{po}_{r,\mathbf{k}}\sigma_y + \varepsilon^{po}_{i,\mathbf{k}}\sigma_x\right)\nu_z\tau_y + \left(\varepsilon^{zo}_{r,\mathbf{k}}\sigma_y + \varepsilon^{zo}_{i,\mathbf{k}}\sigma_x\right)\nu_y\tau_z \\ &+ \left(\varepsilon^{do}_{r,\mathbf{k}}\sigma_y + \varepsilon^{do}_{i,\mathbf{k}}\sigma_x\right)\nu_x\tau_y + \varepsilon^{d}_{r,\mathbf{k}}\nu_x\tau_x + \varepsilon^{d}_{i,\mathbf{k}}\nu_y\tau_y \\ &+ \varepsilon^{p}_{r,\mathbf{k}}\tau_x + \varepsilon^{p}_{i,\mathbf{k}}\sigma_z\tau_y + \varepsilon^{z}_{\mathbf{k}}\nu_x + \lambda_{\mathbf{k}}\end{aligned} \tag{A1}$$

in the basis $[c_{B\uparrow}, c_{R\uparrow}, c_{Y\uparrow}, c_{G\uparrow}, c_{B\downarrow}, c_{R\downarrow}, c_{Y\downarrow}, c_{G\downarrow}]^{\mathrm{T}}$, where B, R, Y, and G correspond to the sublattices of Ir atoms following the convention in Ref. [2]. Here, σ_α, τ_α, and ν_α are Pauli matrices where σ_α is for the $J_{\mathrm{eff}} = 1/2$ effective total angular momentum and $\tau_\alpha(\nu_\alpha)$ is for the sublattices B and R (Y and G) [20]. The matrix elements are defined as

$$\lambda_{\mathbf{k}} = t_{xy}\cos k_x \cos k_y, \tag{A2}$$
$$\varepsilon^{p}_{r,\mathbf{k}} = 2t_p(\cos k_x + \cos k_y), \tag{A3}$$
$$\varepsilon^{p}_{i,\mathbf{k}} = -t'_p(\cos k_x + \cos k_y), \tag{A4}$$
$$\varepsilon^{z}_{\mathbf{k}} = 2t_p \cos k_z, \tag{A5}$$
$$\varepsilon^{zo}_{r,\mathbf{k}} = t^o_z \cos k_z, \tag{A6}$$
$$\varepsilon^{zo}_{i,\mathbf{k}} = -t^o_z \cos k_z, \tag{A7}$$
$$\varepsilon^{d}_{r,\mathbf{k}} = t_d(\cos k_x + \cos k_y)\cos k_z, \tag{A8}$$
$$\varepsilon^{d}_{i,\mathbf{k}} = t'_d(\sin k_x + \sin k_y)\sin k_z, \tag{A9}$$
$$\varepsilon^{po}_{r,\mathbf{k}} = t^o_{1p}\cos k_x + t^o_{2p}\cos k_y, \tag{A10}$$
$$\varepsilon^{po}_{i,\mathbf{k}} = -\left(t^o_{2p}\cos k_x + t^o_{1p}\cos k_y\right), \tag{A11}$$
$$\varepsilon^{do}_{r,\mathbf{k}} = t^o_d \sin k_y \sin k_z, \tag{A12}$$
$$\varepsilon^{do}_{i,\mathbf{k}} = t^o_d \sin k_x \sin k_z. \tag{A13}$$

Here, we exclude symmetry-allowed terms proportional to t_{d1} which do not change the electronic structures both qualitatively and quantitatively due to its tiny magnitude [20]. The TB parameters consistent with the first principles results are presented in Table I. For convenience, we define another set of hopping parameters as $t_0 = t_p$, $t_1 = t'_p$, $t_2 = t^o_z$, $t_3 = t^o_{1p} - t^o_{2p}$, $t_4 = t^o_{1p} + t^o_{2p}$, and $t_5 = t^o_d$, which are used for the analysis of the continuum model. The momentum space is usually spanned by $k_a = k_y + k_x$, $k_b = k_y - k_x$, and $k_c = 2k_z$, where a, b, and c represent orthorhombic axes of the lattice.

This model possesses a ring-shaped zero-energy contour in the $k_b = \pm\pi$ plane described by

$$t_5^2\cos^2\frac{q_a}{2}\cos^2\frac{q_c}{2} = t_3^2\sin^2\frac{q_a}{2} + \left(2t_0^2 + t_2^2\right)\sin^2\frac{q_c}{2}, \tag{A14}$$

where $\mathbf{q} = \mathbf{k} - \mathbf{k}_U$ and $\mathbf{k}_U = (0, -\pi, \pi)$ as shown in Fig. 1(a). On the ring, the energy spectrum is given by $E(\mathbf{q})|_{\mathrm{ring}} = -t_{xy}\sin^2\frac{q_a}{2}$, which is almost nondispersive and can be considered as a nodal line if the ring's size is small ($t_5 \ll |t_3|$).

Around the U point, the continuum Hamiltonian which consists only of leading contributions of $\mathcal{H}^{\mathrm{TB}}$ is given by

$$\begin{aligned}\mathcal{H}^{U} = &\frac{1}{2}(t_4 q_b - t_3 q_a)\sigma_y\nu_z\tau_y - \frac{1}{2}(t_4 q_b + t_3 q_a)\sigma_x\nu_z\tau_y \\ &- \frac{t_2}{2}q_c\sigma_y\nu_y\tau_z + \frac{t_2}{2}q_c\sigma_x\nu_y\tau_z - t_5\sigma_y\nu_x\tau_y \\ &+ t_5\sigma_x\nu_x\tau_y + 2t_0 q_b\tau_x - t_1 q_b\sigma_z\tau_y - t_0 q_c\nu_x \end{aligned} \tag{A15}$$

$$\begin{aligned}= &2t_0 q_b\tau_x - t_0 q_c\nu_x - t_1 q_b\tau_y\sigma_z - \frac{t_3 q_a}{2}\nu_z\tau_y(\sigma_x + \sigma_y) \\ &+ \left(\frac{t_2 q_c}{2}\nu_y\tau_z - \frac{t_4 q_b}{2}\nu_z\tau_y + t_5\nu_x\tau_y\right)(\sigma_x - \sigma_y).\end{aligned} \tag{A16}$$

TABLE I. Tight binding parameters in eV [19].

t_p	t'_p	t_{xy}	t_z	t^o_z	t_d	t'_d	t^o_{1p}	t^o_{2p}	t^o_d
−0.6	−0.15	−0.3	−0.6	0.13	−0.3	0.03	0.1	0.3	0.06

APPENDIX B: EXISTENCE OF ZERO MODES AT $\theta = 0$

When $q_c \leqslant r_c$, the matrix forms of $\mathcal{H}^D_K$ and $\mathcal{H}^D_{K'}$ are given by

$$\mathcal{H}^D_{K(K')} = \begin{pmatrix} \mathbf{h}^+_{K(K')} & \mathbf{g}_\theta \\ \mathbf{g}^\dagger_\theta & \mathbf{h}^-_{K(K')} \end{pmatrix}, \tag{B1}$$

where

$$\mathbf{h}_K^{\pm} = \begin{pmatrix} 0 & v_a(q_a \mp p_a) - i v_b q_b \\ v_a(q_a \mp p_a) + i v_b q_b & 0 \end{pmatrix}, \quad \text{(B2)}$$

$$\mathbf{h}_{K'}^{\pm} = \begin{pmatrix} 0 & v_a(q_a \mp p_a) + i v_b q_b \\ v_a(q_a \mp p_a) - i v_b q_b & 0 \end{pmatrix}, \quad \text{(B3)}$$

and

$$\mathbf{g}_\theta = v_c q_c \begin{pmatrix} -i\sin\theta & 2\sin^2\frac{\theta}{2} \\ 2\cos^2\frac{\theta}{2} & i\sin\theta \end{pmatrix}. \quad \text{(B4)}$$

For the Landau level quantization, we define ladder operators as

$$a_+ = \frac{l_B}{\sqrt{2}v_f}[v_a(q_a - p_a) + i v_b q_b], \quad \text{(B5)}$$

$$a_- = \frac{l_B}{\sqrt{2}v_f}[v_a(q_a + p_a) + i v_b q_b], \quad \text{(B6)}$$

where $v_f = \sqrt{v_a v_b}$ and $p_a = \sqrt{[2t_5^2 - (v_c q_c)^2]/v_a^2}$. The upper and lower layer's ladder operators satisfy $a_+ = a_- - s_0$, where $s_0 = \sqrt{2} v_a l_B p_a / v_f$. Their eigenfunctions are related to each other by $u_n^+(y) = u_n^-(y - 2p_a l_B^2)$ due to the momentum shift $2p_a$ between Dirac cones in the upper and lower layers. Then, under the magnetic field, the Hamiltonian matrix for $\theta = 0$ is expressed as

$$\mathcal{H}_K^D = \begin{pmatrix} 0 & \frac{\sqrt{2}v_f}{l_B}a_+^\dagger & 0 & 0 \\ \frac{\sqrt{2}v_f}{l_B}a_+ & 0 & 2v_c q_c & 0 \\ 0 & 2v_c q_c & 0 & \frac{\sqrt{2}v_f}{l_B}a_-^\dagger \\ 0 & 0 & \frac{\sqrt{2}v_f}{l_B}a_- & 0 \end{pmatrix} \quad \text{(B7)}$$

and

$$\mathcal{H}_{K'}^D = \begin{pmatrix} 0 & \frac{\sqrt{2}v_f}{l_B}a_+ & 0 & 0 \\ \frac{\sqrt{2}v_f}{l_B}a_+^\dagger & 0 & 2v_c q_c & 0 \\ 0 & 2v_c q_c & 0 & \frac{\sqrt{2}v_f}{l_B}a_- \\ 0 & 0 & \frac{\sqrt{2}v_f}{l_B}a_-^\dagger & 0 \end{pmatrix}. \quad \text{(B8)}$$

While these Hamiltonians are not solvable analytically in general, they allow analytic forms of zero-energy eigenfunctions as follows. First, when $q_c < r_c$,

$$\psi_{K,1}^0 = \begin{pmatrix} u_0^+ \\ 0 \\ 0 \\ 0 \end{pmatrix} \quad \text{and} \quad \psi_{K,2}^0 = c_0 \begin{pmatrix} u_0^- \\ 0 \\ \gamma_0 u_0^- \\ 0 \end{pmatrix} \quad \text{(B9)}$$

for the K valley, and

$$\psi_{K',1}^0 = \begin{pmatrix} 0 \\ 0 \\ 0 \\ u_0^- \end{pmatrix} \quad \text{and} \quad \psi_{K',2}^0 = c_0 \begin{pmatrix} 0 \\ -\gamma_0 u_0^+ \\ 0 \\ u_0^+ \end{pmatrix} \quad \text{(B10)}$$

for the K' valley, where $\gamma_0 = p_a v_a/(v_c q_c)$ and $c_0 = (1 + \gamma_0^2)^{-1/2}$. If $q_c = r_c$, p_a vanishes and some of the above solutions are not linearly independent to each other. In the case, we have another set of four zero modes as

$$\psi_{K,1}^0 = \begin{pmatrix} u_0 \\ 0 \\ 0 \\ 0 \end{pmatrix} \quad \text{and} \quad \psi_{K,2}^0 = c_1 \begin{pmatrix} \gamma_1 u_1 \\ 0 \\ u_0 \\ 0 \end{pmatrix} \quad \text{(B11)}$$

for the K valley, and

$$\psi_{K',1}^0 = \begin{pmatrix} 0 \\ 0 \\ 0 \\ u_0 \end{pmatrix} \quad \text{and} \quad \psi_{K',2}^0 = c_1 \begin{pmatrix} 0 \\ u_0 \\ 0 \\ \gamma_1 u_1 \end{pmatrix} \quad \text{(B12)}$$

for the K' valley, where $\gamma_1 = -\sqrt{2} v_c l_B q_c / v_f$ and $c_1 = (1 + \gamma_1^2)^{-1/2}$. Here, we use the single kind of the SHO wave function u_n since a_+ and a_- are identical in this case.

When $q_c > r_c$, because the plane of the nodal line is changed to the $k_a = 0$ plane, the expressions for the Hamiltonians are also different from the $q_c < r_c$ case. They are given by

$$\mathbf{h}_K^{\pm} = \begin{pmatrix} m_0 q_c & v_a q_a - i v_b(q_b \mp p_b) \\ v_a q_a + i v_b(q_b \mp p_b) & -m_0 q_c \end{pmatrix}, \quad \text{(B13)}$$

$$\mathbf{h}_{K'}^{\pm} = \begin{pmatrix} m_0 q_c & v_a q_a + i v_b(q_b \mp p_b) \\ v_a q_a - i v_b(q_b \mp p_b) & -m_0 q_c \end{pmatrix}, \quad \text{(B14)}$$

and

$$\mathbf{g}_\theta = \sqrt{2} t_5 \begin{pmatrix} 0 & 1 \\ 1 & 0 \end{pmatrix}, \quad \text{(B15)}$$

where $m_0 = v_c \sin\theta$ and $p_b = \sqrt{v_a} q_c / 2v_b^2$. The sign of the on-site interaction is opposite between layers and we have two fictitious interlayer couplings. In this case, we define just a single ladder operator as

$$b = \frac{l_B}{\sqrt{2}v_f}(v_a q_a + i v_b q_b). \quad \text{(B16)}$$

Then, for $\theta = 0$ case where the mass terms are vanishing, we have

$$\mathcal{H}_K^D = \begin{pmatrix} 0 & B_-^\dagger & 0 & \sqrt{2}t_5 \\ B_- & 0 & \sqrt{2}t_5 & 0 \\ 0 & \sqrt{2}t_5 & 0 & B_+^\dagger \\ \sqrt{2}t_5 & 0 & B_+ & 0 \end{pmatrix} \quad \text{(B17)}$$

at the K valley, and

$$\mathcal{H}_K^D = \begin{pmatrix} 0 & B_- & 0 & \sqrt{2}t_5 \\ B_-^\dagger & 0 & \sqrt{2}t_5 & 0 \\ 0 & \sqrt{2}t_5 & 0 & B_+ \\ \sqrt{2}t_5 & 0 & B_+^\dagger & 0 \end{pmatrix} \quad \text{(B18)}$$

at the K' valley, where

$$B_\pm = \frac{\sqrt{2}v_f}{l_B} b \pm i v_b p_b. \quad \text{(B19)}$$

In the case where $q_c > r_c$, we do not have simple solutions such as the above ($q_c < r_c$ case). Instead, we try a infinite sum of SHO wave functions in the form

$$\psi = \sum_{n=0}^{\infty} \begin{pmatrix} c_n^{A_+} & c_n^{B_+} & c_n^{A_1} & c_n^{B_-} \end{pmatrix}^{\mathrm{T}} u_n \tag{B20}$$

whose coefficients satisfy

$$\varepsilon \begin{pmatrix} c_n^{A_+} \\ c_n^{A_-} \end{pmatrix} = \mathbf{T}^{\dagger} \begin{pmatrix} c_n^{B_+} \\ c_n^{B_-} \end{pmatrix} + \frac{\sqrt{2n} v_f}{l_{\mathrm{B}}} \begin{pmatrix} c_{n-1}^{B_+} \\ c_{n-1}^{B_-} \end{pmatrix}, \tag{B21}$$

$$\varepsilon \begin{pmatrix} c_n^{B_+} \\ c_n^{B_-} \end{pmatrix} = \mathbf{T} \begin{pmatrix} c_n^{A_+} \\ c_n^{A_-} \end{pmatrix} + \frac{\sqrt{2(n+1)} v_f}{l_{\mathrm{B}}} \begin{pmatrix} c_{n+1}^{A_+} \\ c_{n+1}^{A_-} \end{pmatrix} \tag{B22}$$

at the K valley, and

$$\varepsilon \begin{pmatrix} c_n^{A_+} \\ c_n^{A_-} \end{pmatrix} = \mathbf{T} \begin{pmatrix} c_n^{B_+} \\ c_n^{B_-} \end{pmatrix} + \frac{\sqrt{2(n+1)} v_f}{l_{\mathrm{B}}} \begin{pmatrix} c_{n+1}^{B_+} \\ c_{n+1}^{B_-} \end{pmatrix}, \tag{B23}$$

$$\varepsilon \begin{pmatrix} c_n^{B_+} \\ c_n^{B_-} \end{pmatrix} = \mathbf{T}^{\dagger} \begin{pmatrix} c_n^{A_+} \\ c_n^{A_-} \end{pmatrix} + \frac{\sqrt{2n} v_f}{l_{\mathrm{B}}} \begin{pmatrix} c_{n-1}^{A_+} \\ c_{n-1}^{A_-} \end{pmatrix} \tag{B24}$$

at the K' valley. Here,

$$\mathbf{T} = \begin{pmatrix} -i v_b p_b & \sqrt{2} t_5 \\ \sqrt{2} t_5 & i v_b p_b \end{pmatrix}. \tag{B25}$$

If we assume $\varepsilon = 0$, one can decouple the sublattices into $\{A_+, A_-\}$ and $\{B_+, B_-\}$ and we have diverging sequences on the $B(A)$ sublattice at the $K(K')$ valley given by

$$\begin{pmatrix} c_n^{B_+} \\ c_n^{B_-} \end{pmatrix} = -\frac{\sqrt{2n} v_f}{l_{\mathrm{B}}} \begin{pmatrix} i v_b p_b & \sqrt{2} t_5 \\ \sqrt{2} t_5 & -i v_b p_b \end{pmatrix}^{-1} \begin{pmatrix} c_{n-1}^{B_+} \\ c_{n-1}^{B_-} \end{pmatrix} \tag{B26}$$

at the K valley, and

$$\begin{pmatrix} c_n^{A_+} \\ c_n^{A_-} \end{pmatrix} = -\frac{\sqrt{2n} v_f}{l_{\mathrm{B}}} \begin{pmatrix} i v_b p_b & \sqrt{2} t_5 \\ \sqrt{2} t_5 & -i v_b p_b \end{pmatrix}^{-1} \begin{pmatrix} c_{n-1}^{A_+} \\ c_{n-1}^{A_-} \end{pmatrix} \tag{B27}$$

at the K' valley. Due to the multiplying factor $\sqrt{n}$ between consecutive coefficients, the sequence cannot avoid the divergence. On the other hand, there are two possible zero modes at each valley which obey the following converging sequences,

$$\begin{pmatrix} c_{n+1}^{A_+} \\ c_{n+1}^{A_-} \end{pmatrix} = \frac{1}{\sqrt{n+1}} \mathbf{T} \begin{pmatrix} c_n^{A_+} \\ c_n^{A_-} \end{pmatrix} \tag{B28}$$

at the K valley, and

$$\begin{pmatrix} c_{n+1}^{B_+} \\ c_{n+1}^{B_-} \end{pmatrix} = \frac{1}{\sqrt{n+1}} \mathbf{T} \begin{pmatrix} c_n^{B_+} \\ c_n^{B_-} \end{pmatrix} \tag{B29}$$

at the K' valley. If we choose the two eigenvectors of the matrix $\mathbf{T}$ as the initial vectors $(c_0^{A_+}, c_0^{A_-})^{\mathrm{T}}$ for the K valley and $(c_0^{B_+}, c_0^{B_-})^{\mathrm{T}}$ for the K' valley, due to the multiplying factor $1/\sqrt{n+1}$, the sequences vanish faster than exponentially in the $n \to \infty$ limit so that they are normalizable. This gives us four zero-energy solutions, two from the A sites at the K valley and the other two from the B sites at the K' valley.

[1] K. S. Novoselov, A. K. Geim, S. V. Morozov, D. Jiang, M. I. Katsnelson, I. V. Grigorieva, S. V. Dubonos, and A. A. Firsov, Nature (London) **438**, 197 (2005).

[2] Y. Zhang, Y.-W. Tan, H. L. Stormer, and P. Kim, Nature (London) **438**, 201 (2005).

[3] A. H. Castro Neto, F. Guinea, N. M. R. Peres, K. S. Novoselov, and A. K. Geim, Rev. Mod. Phys. **81**, 109 (2009).

[4] E. McCann and V. I. Falko, Phys. Rev. Lett. **96**, 086805 (2006).

[5] K.-Y. Yang, Y.-M. Lu, and Y. Ran, Phys. Rev. B **84**, 075129 (2011).

[6] B.-J. Yang and Y. B. Kim, Phys. Rev. B **82**, 085111 (2010).

[7] W. Witczak-Krempa and Y. B. Kim, Phys. Rev. B **85**, 045124 (2012).

[8] E.-G. Moon, C. Xu, Y. B. Kim, and L. Balents, Phys. Rev. Lett. **111**, 206401 (2013).

[9] S. Raghu, X.-L. Qi, C. Honerkamp, and S.-C. Zhang, Phys. Rev. Lett. **100**, 156401 (2008).

[10] J.-W. Rhim and Y. B. Kim, Phys. Rev. B **91**, 115124 (2015).

[11] A. A. Burkov and L. Balents, Phys. Rev. Lett. **107**, 127205 (2011).

[12] X. Wan, A. M. Turner, A. Vishwanath, and S. Y. Savrasov, Phys. Rev. B **83**, 205101 (2011).

[13] G. Xu, H. Weng, Z. Wang, X. Dai, and Z. Fang, Phys. Rev. Lett. **107**, 186806 (2011).

[14] S. M. Young, S. Zaheer, J. C. Y. Teo, C. L. Kane, E. J. Mele, and A. M. Rappe, Phys. Rev. Lett. **108**, 140405 (2012).

[15] Z. Wang, Y. Sun, X.-Q. Chen, C. Franchini, G. Xu, H. Weng, X. Dai, and Z. Fang, Phys. Rev. B **85**, 195320 (2012).

[16] A. A. Burkov, M. D. Hook, and L. Balents, Phys. Rev. B **84**, 235126 (2011).

[17] M. Z. Hasan and C. L. Kane, Rev. Mod. Phys. **82**, 3045 (2010); X.-L. Qi and S.-C. Zhang, *ibid.* **83**, 1057 (2011).

[18] S. Matsuura, P.-Y. Chang, A. P. Schnyder, and S. Ryu, New J. Phys. **15**, 065001 (2013).

[19] J.-M. Carter, V. V. Shankar, M. A. Zeb, and H.-Y. Kee, Phys. Rev. B **85**, 115105 (2012).

[20] Y. Chen, Y.-M. Lu, and H.-Y. Kee, Nat. Commun. **6**, 6593 (2015).

[21] H.-S. Kim, Y. Chen, and H.-Y. Kee, Phys. Rev. B **91**, 235103 (2015).

[22] Y. Kim, B. J. Wieder, C. L. Kane, and A. M. Rappe, Phys. Rev. Lett. **115**, 036806 (2015).

[23] L. S. Xie, L. M. Schoop, E. M. Seibel, Q. D. Gibson, W. Xie, and R. J. Cava, APL Mater. **3**, 083602 (2015).

[24] M. Zeng, C. Fang, G. Chang, Y.-A. Chen, T. Hsieh, A. Bansil, H. Lin, and L. Fu, arXiv:1504.03492.

[25] S.-Y. Xu, N. Alidoust, I. Belopolski, C. Zhang, G. Bian, T.-R. Chang, H. Zheng, V. Strokov, D. S. Sanchez, G. Chang, Z. Yuan, D. Mou, Y. Wu, L. Huang, C.-C. Lee, S.-M. Huang, B. Wang, A. Bansil, H.-T. Jeng, T. Neupert, A. Kaminski, H. Lin, S. Jia, and M. Z. Hasan, arXiv:1504.01350.

[26] H. Weng, Y. Liang, Q. Xu, Y. Rui, Z. Fang, X. Dai, and Y. Kawazoe, Phys. Rev. B **92**, 045108 (2015).
[27] R. Yu, H. Weng, Z. Fang, X. Dai, and X. Hu, Phys. Rev. Lett. **115**, 036807 (2015).
[28] H. Weng, C. Fang, Z. Fang, B. A. Bernevig, and X. Dai, Phys. Rev. X **5**, 011029 (2015).
[29] L. Zhang, Y. B. Chen, B. Zhang, J. Zhou, S. Zhang, Z. Gu, S. Yao, and Y. Chen, J. Phys. Soc. Jpn. **83**, 054707 (2014).
[30] S. Murakami, N. Nagaosa, and S.-C. Zhang, Phys. Rev. B **69**, 235206 (2004).
[31] S. S. Pershoguba and V. M. Yakovenko, Phys. Rev. B **82**, 205408 (2010).
[32] S. S. Pershoguba, D. S. L. Abergel, V. M. Yakovenko, and A. V. Balatsky, Phys. Rev. B **91**, 085418 (2015).
[33] L. Petersen and P. Hedegrd, Surf. Sci. **459**, 49 (2000).
[34] V. Halpern, J. Phys. C: Solid State Phys. **4**, L369 (1971).
[35] Unlike the case $q_c < r_c$, when $q_c > r_c$, the artificial parallel magnetic field cannot keep the flatness of the zero modes at $\theta = 0$ due to the mass terms in each Dirac Hamiltonian. As a result, we have large splittings between central Landau levels, as shown in Figs. 2(a) and 2(b), even if θ is small.
[36] B. I. Halperin, Jpn. J. Appl. Phys. Suppl. **26**, 1913 (1987).
[37] B. A. Bernevig, T. L. Hughes, S. Raghu, and D. P. Arovas, Phys. Rev. Lett. **99**, 146804 (2007).